

Theoretical insights of codoping to modulate electronic structure of TiO_2 and SrTiO_3 for enhanced photocatalytic efficiency

Manish Kumar,* Pooja Basera, Shikha Saini, and Saswata Bhattacharya†
*Department of Physics, Indian Institute of Technology Delhi,
 New Delhi 110016, India*

(Dated: September 13, 2021)

TiO_2 and SrTiO_3 are well known materials in the field of photocatalysis due to their exceptional electronic structure, high chemical stability, non-toxicity and low cost. However, owing to the wide band gap, these can be utilized only in the UV region. Thus, it's necessary to expand their optical response in visible region by reducing their band gap through doping with metals, nonmetals or the combination of different elements, while retaining intact the photocatalytic efficiency. We report here, the codoping of a metal and a nonmetal in anatase TiO_2 and SrTiO_3 for efficient photocatalytic water splitting using hybrid density functional theory and *ab initio* atomistic thermodynamics. The latter ensures to capture the environmental effect to understand thermodynamic stability of the charged defects at a realistic condition. We have observed that the charged defects are stable in addition to neutral defects in anatase TiO_2 and the codopants act as donor as well as acceptor depending on the nature of doping (p-type or n-type). However, the most stable codopants in SrTiO_3 mostly act as donor. Our results reveal that despite the response in visible light region, the codoping in TiO_2 and SrTiO_3 cannot always enhance the photocatalytic activity due to either the formation of recombination centers or the large shift in the conduction band minimum or valence band maximum. Amongst various metal-nonmetal combinations, $\text{Mn}_{\text{Ti}}\text{S}_\text{O}$ (i.e. Mn is substituted at Ti site and S is substituted at O site), S_O in anatase TiO_2 and $\text{Mn}_{\text{Ti}}\text{S}_\text{O}$, $\text{Mn}_{\text{Sr}}\text{N}_\text{O}$ in SrTiO_3 are the most potent candidates to enhance the photocatalytic efficiency of anatase TiO_2 and SrTiO_3 under visible light irradiation.

I. INTRODUCTION

Semiconductor-based photocatalysts are seeking the attention ascribed to their potential in utilizing the solar energy to cater to the current energy demand of the world and also, serve the purpose of pollutant degradation [1–8]. Anatase TiO_2 and SrTiO_3 are two of the metal oxides that can be used in photocatalytic water splitting [4, 9–23] owing to their suitable band edge positions. However, they could only exploit the UV irradiation of the solar spectrum attributed to their wide band gap of ~ 3.2 eV. This leads to the low photocatalytic efficiency and limits their application at a commercial level. An efficient photocatalyst should have congenial band gap such that it is wide enough to straddle the redox potential of a desired compound and narrow enough to absorb the visible light of the solar spectrum. However, despite after significant research endeavors, finding the same has never been easy both experimentally as well as theoretically. Therefore, there is justified interest to reduce the band gap and induce visible light response by means of doping with metals [24–30], nonmetals [31–39] or their combination [40–46]. Although the doping can tune the band gap [9–17], many a time the band edge positions also get changed and the localized deep trap states occur in forbidden region leading to faster recombination. As a consequence, the photocatalytic efficiency gets degraded.

Therefore, we need to ensure the suitable band edge positions as well as the passivation of midgap trap states (i.e. recombination centers).

The conduction band minimum (CBM) lies ~ 0.4 eV and 0.8 eV above the reduction potential of water for anatase TiO_2 [47] and SrTiO_3 [48], respectively, concomitant with the reduction of water to produce hydrogen under UV irradiation. The transition metal dopant shifts the CBM downwards (towards valence band maximum (VBM)) and hence results in deterioration of reduction power. On the other hand, in case of nonmetal dopant, the band gap reduction takes place by elevating the VBM. However, many a time localized deep trap states appear in forbidden region in both the aforementioned cases. Moreover, the nonmetal doped systems are unstable against exposure to light irradiation [49]. Therefore, despite the visible light absorption, none of the monodopants (be it metal or nonmetal) are usually suitable for photocatalytic water splitting. This has motivated us to codeope the system. The codoping of a metal and a nonmetal is one of the prominent solutions to passivate the trap states and form the shallow impurity states [49]. Note that for maximum efficiency, the band gap should be ~ 2 eV [50, 51]. With the aid of codoping, the band gap could be tailored such that it induces visible light absorption while retaining the redox powers and thus, enhances the photocatalytic efficiency [52]. Note that the experimental synthesis of individual monodopants (i.e. N, S, Rh and Mn) in TiO_2 as well as SrTiO_3 have already been done [37, 38, 53–59]. A very few experimental studies also exist on N-Mn and S-Mn codoped TiO_2 as well [60, 61]. However, for the codoping (viz. N-Mn,

* manish.kumar@physics.iitd.ac.in

† saswata@physics.iitd.ac.in

N-Rh, S-Mn and S-Rh) in bulk SrTiO₃ and N-Rh, S-Rh in anatase TiO₂, any experimental or theoretical reports are hitherto unknown.

In this article, we have studied the role of codopants (N-Mn, N-Rh, S-Mn and S-Rh) in anatase TiO₂ and SrTiO₃ for enhancing the photocatalytic efficiency. We have shown in Ref. [62, 63] that the substitutional doping is more favorable than the interstitial in TiO₂ as well as SrTiO₃. Therefore, we have chosen only the substitutional positions (i.e. metal at Ti or Sr site and nonmetal at O site) for codoping. First, we have determined the thermodynamic stability of codoped TiO₂ and SrTiO₃ under the framework of hybrid density functional theory (DFT) [64, 65] and *ab initio* thermodynamics at realistic conditions (temperature (T), partial pressure of oxygen (p_{O_2}) and doping) [66]. Next, the electronic structure has been analyzed to get insight about the defect states. Further, we have calculated the optical properties to compare the spectral response of all the defected configurations w.r.t pristine counterpart. To explore the best set of codoped combinations for photocatalytic water splitting, the band edge alignment has been carefully carried out. Finally, under codoping, the effective mass has been determined to understand the effect on mobility of positive ions.

II. METHODOLOGY

We have performed the DFT calculations as implemented in Vienna *ab initio* simulation package (VASP) [67, 68]. The projector-augmented wave (PAW) pseudopotentials [69] have been used to describe the interactions between electrons and ions for all the species. For the energy calculations, hybrid exchange-correlational (xc) functional HSE06 [70] is used. The exact exchange fractions in HSE06 functional used for TiO₂ and SrTiO₃ are 22% and 28%, respectively (see SI ref. [62, 63] for validation of exact exchange fraction). The band gap of 3.15 eV and 3.28 eV are reproduced for TiO₂ and SrTiO₃ respectively, which are well in agreement with the experimental values [71, 72]. To make the defect to be localized, we have used $2 \times 2 \times 1$ (48-atom) and $2 \times 2 \times 2$ (40-atom) supercells by replication of TiO₂ and SrTiO₃ unit cells respectively. The k-grid for Brillouin zone sampling is generated using Monkhorst-Pack [73] scheme and all results are checked for convergence w.r.t. the mesh size ($4 \times 4 \times 4$). The electronic self-consistency loop for the total energy is converged with a threshold of 0.01 meV. An energy cutoff of 600 eV is used for the plane wave basis set. Note that the spin-polarized calculations have been carried out since the doped systems contain unpaired electrons.

III. RESULTS

A. Stability of codoped TiO₂ and SrTiO₃

The stability has been determined by calculating the defect formation energy using hybrid DFT and *ab initio* thermodynamics [66, 74, 75]. The defect configuration, having minimum formation energy, is the most stable defect. For a defect X with charge state q , the formation energy $E_f(X^q)$ is evaluated as follow [62, 66, 76]:

$$E_f(X^q) = E_{\text{tot}}(X^q) - E_{\text{tot}}(\text{pristine}^0) - \sum_i n_i \mu_i + q(\mu_e + \text{VBM} + \Delta V), \quad (1)$$

where $E_{\text{tot}}(X^q)$ and $E_{\text{tot}}(\text{pristine}^0)$ are the energies of defected supercell (charged) and pristine supercell (neutral), respectively, calculated using hybrid DFT. n_i is the number of species i added to or removed from the pristine supercell and μ_i 's are the corresponding chemical potentials, which is selected with reference to the total energy ($E_{\text{tot}}(i^0)$) of species i . Therefore, $\mu_i = \Delta\mu_i + E_{\text{tot}}(i)$ ($i = \text{N, S, O, Mn, Rh, Sr, or Ti}$), where $\Delta\mu_i$'s are chosen according to the environmental growth conditions. μ_e is the chemical potential of the electron, which is the energy required to exchange electrons between the system and the electrons' reservoir. It is varied from VBM to CBM of the pristine supercell. ΔV is the core level alignment between pristine neutral and defected supercell.

The chemical potential of a species incorporates the effect of temperature and pressure. For oxygen, the $\Delta\mu_{\text{O}}$ as a function of temperature (T) and the partial pressure of oxygen (p_{O_2}) is calculated as follow [74]:

$$\begin{aligned} \Delta\mu_{\text{O}}(T, p_{\text{O}_2}) = & \frac{1}{2} \left[-k_{\text{B}}T \ln \left[\left(\frac{2\pi m}{h^2} \right)^{\frac{3}{2}} (k_{\text{B}}T)^{\frac{5}{2}} \right] \right. \\ & + k_{\text{B}}T \ln p_{\text{O}_2} - k_{\text{B}}T \ln \left(\frac{8\pi^2 I_A k_{\text{B}}T}{h^2} \right) \\ & + k_{\text{B}}T \ln \left[1 - \exp \left(\frac{-h\nu_{\text{OO}}}{k_{\text{B}}T} \right) \right] \\ & \left. - k_{\text{B}}T \ln \mathcal{M} + k_{\text{B}}T \ln \sigma \right], \end{aligned} \quad (2)$$

where m is the mass, I_A is the moment of inertia of O₂ molecule, ν_{OO} is the O-O stretching frequency, \mathcal{M} is the spin multiplicity and σ is the symmetry number.

For TiO₂ and SrTiO₃, the equilibrium growth conditions are:

$$\begin{aligned} \Delta\mu_{\text{Ti}} + 2\Delta\mu_{\text{O}} &= \Delta H_{\text{f}}(\text{TiO}_2), \\ \Delta\mu_{\text{Sr}} + \Delta\mu_{\text{Ti}} + 3\Delta\mu_{\text{O}} &= \Delta H_{\text{f}}(\text{SrTiO}_3), \end{aligned} \quad (3)$$

respectively. Here, ΔH_{f} denotes the enthalpy of formation. The bounds are imposed on chemical potentials to restrain the formation of secondary phases (viz. TiO₂,

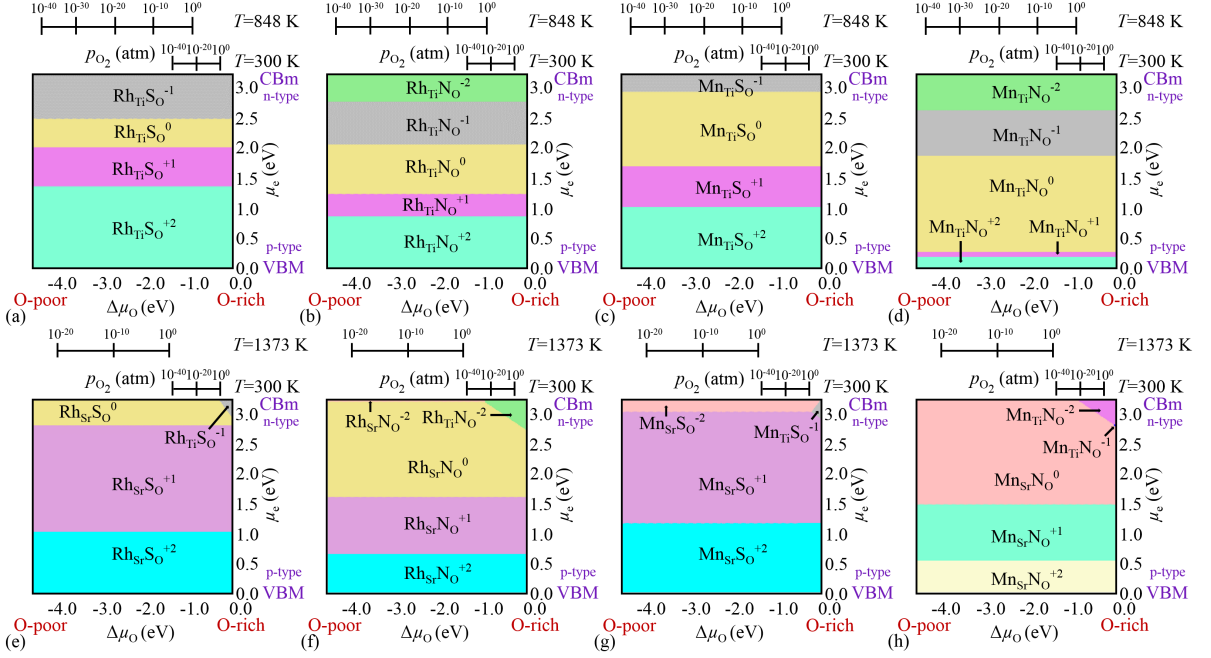


FIG. 1. 3D phase diagram that shows the most stable phases of (a) RhTiSO , (b) RhTiNO , (c) MnTiSO and (d) MnTiNO codoped TiO_2 charged configurations, and (e) S-Rh, (f) N-Rh, (g) S-Mn and (h) N-Mn [63] codoped SrTiO_3 charged configurations with minimum formation energy as a function of $\Delta\mu_{\text{O}}$ and μ_e . Here, $\Delta\mu_{\text{O}}$ (on x-axis) is varied according to environmental growth conditions (T and p_{O_2} (on top axes)) and μ_e (on y-axis) is varied from VBM to CBm of pristine system. The experimental growth conditions for TiO_2 are $T = 848$ K, $p_{\text{O}_2} = 2.6 \times 10^{-8}$ atm [77] and for SrTiO_3 are $T = 1373$ K, $p_{\text{O}_2} = 1$ atm [36].

SrO in SrTiO_3) as follow:

$$\begin{aligned} \Delta\mu_{\text{Ti}} + 2\Delta\mu_{\text{O}} &\leq \Delta H_{\text{f}}(\text{TiO}_2), \\ \Delta\mu_{\text{Sr}} + \Delta\mu_{\text{O}} &\leq \Delta H_{\text{f}}(\text{SrO}), \\ \Delta\mu_i &\leq 0. \end{aligned} \quad (4)$$

The chemical potentials are determined by imposing bounds on the formation of the precursors (MnO_2 , TiO_2 , TiS_2 , Rh_2O_3), and the aforementioned Eqs. 3 and 4.

In our previous findings, we have seen that the substitutional defect is more favorable in comparison to interstitial and also, observed that the monodopants in general are not suitable for photocatalytic application [62, 63]. Therefore, we have considered here the codoped cases (metal (Rh or Mn) substituted at Ti or Sr site, and non-metal (N or S) substituted at O site). Fig. 1 shows the stable phases of codoped TiO_2 and SrTiO_3 with minimum formation energy. These stable phases include charged defects in addition to neutral defects due to the uncompensated charge. The positive charge states are stable near VBM (in p-type host), whereas the negative charge states are stable near CBM (in n-type host). The RhTiSO and MnTiSO codoped TiO_2 could be stable in +2, +1, 0, and -1 charge states [see Figs. 1(a) and 1(c)]. These codopants will act as donor in p-type host (near VBM), and acceptor in n-type host (near CBM). The charge state -2 is not stable in both the cases. As these transition metals have partially filled d-orbitals, it could accept electrons from the host as well as donate electrons

to the host. Figs. 1(b) and 1(d) show that RhTiNO and MnTiNO codoped TiO_2 will be stable in -2 charge state in addition to +2, +1, 0 and -1, since N has one electron less than O, it could accept one electron extra in comparison to S (S has same number of valence electrons as for O). In MnTiSO and MnTiNO codoped TiO_2 , for a large range of μ_e , neutral charge state is more favorable. The Sr site is more favorable than Ti site for substitution in SrTiO_3 [see Figs. 1(e-h)]. The Ti site could be substituted in O-rich (Ti-poor) conditions near CBM (in n-type host). Mostly, RhSrSO , RhSrNO , MnSrSO , and MnSrNO codopants act as donor as they are stable in +2 and +1 charge states for a wide range of μ_e or in neutral charge state. However, when metal is substituted at the Ti position, the defect configuration will act as an acceptor. Similar to the codoped TiO_2 , the RhTiNO , and MnTiNO codoped SrTiO_3 will get stabilized after accepting one extra electron in comparison to RhTiSO , and MnTiSO .

B. Electronic density of states (DOS)

The defect states could be seen by means of electronic density of states. Fig. 2 shows the atom projected density of states for pristine and codoped TiO_2 as well as SrTiO_3 . In the pristine systems, near Fermi level, the valence band is contributed by O 2p orbitals and the conduction band is contributed by Ti 3d orbitals [see

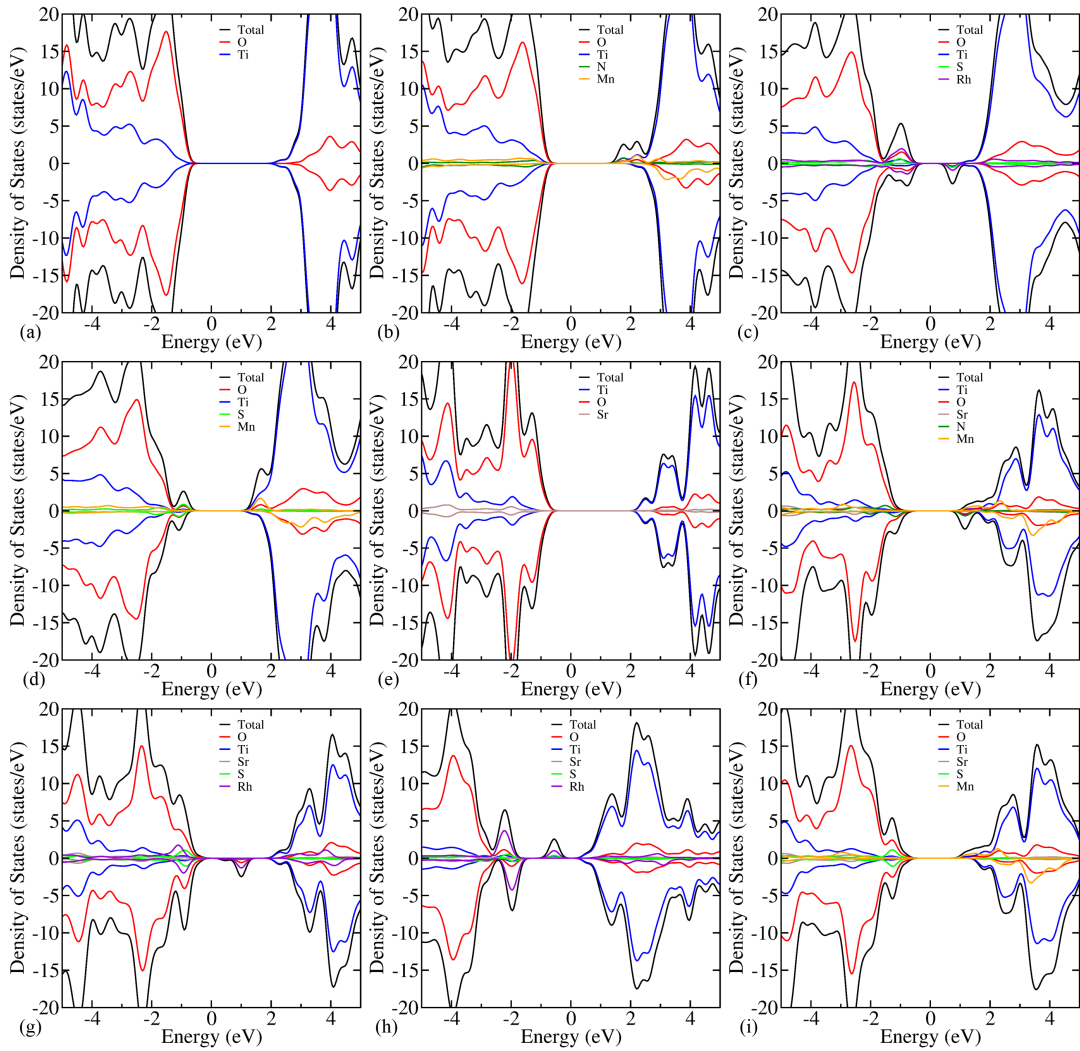


FIG. 2. Atom projected density of states of (a) pristine TiO_2 , (b) $\text{Mn}_{\text{Ti}}\text{NO}$, (c) $\text{Rh}_{\text{Ti}}\text{SO}$, (d) $\text{Mn}_{\text{Ti}}\text{SO}$ codoped TiO_2 , and (e) pristine SrTiO_3 , (f) $\text{Mn}_{\text{Ti}}\text{NO}$ [63], (g) $\text{Rh}_{\text{Ti}}\text{SO}$, (h) $\text{Rh}_{\text{Sr}}\text{SO}$, and (i) $\text{Mn}_{\text{Ti}}\text{SO}$ codoped SrTiO_3 .

Figs. 2(a) and 2(e)]. The DOS is symmetric w.r.t. the spin alignments ascribed to the paired electrons in the system. On doping, the DOS becomes asymmetric attributable to unpaired electrons. The deep trap states arise in N_{O} , Rh_{Ti} and $\text{Rh}_{\text{Ti}}\text{NO}$ doped TiO_2 , that increase the recombination rate and deteriorate the photocatalytic efficiency [see Figs. S1(a), S1(d) and S1(e)]. There is very slight reduction in band gap for Mn_{Ti} doped TiO_2 . Hence, it's not inducing the effective visible light absorption [see Fig. S1(c)]. In $\text{Mn}_{\text{Ti}}\text{NO}$ codoped TiO_2 , the N orbitals and Mn orbitals shift down the CBm, leading to the reduction in band gap and induce the visible light absorption [see Fig. 2(b)]. However, this shift will lower down the CBm and thus, not efficient for reduction of water to produce hydrogen. The VBM is elevated in $\text{Rh}_{\text{Ti}}\text{SO}$ codoped TiO_2 , which is caused by the S and Rh orbitals contribution [see Fig. 2(c)]. Furthermore, the CBm is also shifted down due to the unoccupied states of S and Rh orbitals. Therefore, despite its spectral re-

sponse in visible region, it cannot be used for producing oxygen via water reduction ascribed to the large shift in VBM. The band gap reduction is induced by the S orbitals in S_{O} doped TiO_2 as the S orbitals energies lie higher than the N orbitals [see Fig. S1(b)]. Also, in $\text{Mn}_{\text{Ti}}\text{SO}$ codoped TiO_2 , the S orbitals elevate the VBM as they have higher energy than the O orbitals and the Mn orbitals contribute to CBm [see Fig. 2(d)]. This will enhance the photocatalytic efficiency, as the band gap becomes 2.2 eV in both the aforementioned cases and the band edges straddle the redox potentials of water.

For SrTiO_3 , N_{O} and S_{O} behave similar to the case of N_{O} and S_{O} monodoped TiO_2 [see Figs. S1(f) and S1(g)]. However, the reduction in band gap for S_{O} is small in comparison to S_{O} doped TiO_2 . S_{O} doped SrTiO_3 has the band gap of 2.59 eV and hence, responses to visible light irradiation. For Mn_{Ti} monodoped SrTiO_3 , the Mn orbital contributes to the CBm and lowers down it [see Fig. S1(h)]. Therefore, its spectral response expands

to visible light irradiation (band gap is 2.57 eV). In Rh_{T_i} monodoped SrTiO_3 , the unoccupied states of Rh orbitals appear at VBM, and the difference between highest occupied and lowest unoccupied state is 0.23 eV [see Fig. S1(i)]. Thus, it is not a promising candidate for enhanced photocatalytic activity. The lowering of CBm in Rh_{S_r} is occurred due to the Rh localized states contribution to CBm and therefore, it doesn't have enough reduction power to produce hydrogen via water splitting [see Fig. S1(j)]. There is no reduction in band gap for Mn_{S_r} monodoped SrTiO_3 , as the Mn orbitals contribute deep inside the valence and conduction band [see Fig. S1(k)]. Likewise $\text{Mn}_{\text{T}_i}\text{N}_\text{O}$ codoped TiO_2 , the reduction in band gap of $\text{Mn}_{\text{T}_i}\text{N}_\text{O}$ codoped SrTiO_3 is occurred by lowering of the CBm as well as elevation of the VBM [see Fig. 2(f)]. However, the shift in CBm is large enough such that its reduction power is deteriorated. In $\text{Rh}_{\text{T}_i}\text{S}_\text{O}$ and $\text{Rh}_{\text{S}_r}\text{S}_\text{O}$ codoped SrTiO_3 , the deep trap states arise in the forbidden region, that increase the recombination of photogenerated charge carriers and thus, degrade the photocatalytic activity [see Figs. 2(g) and 2(h)]. Since there is occurrence of trap states in $\text{Rh}_{\text{T}_i}\text{N}_\text{O}$ and $\text{Mn}_{\text{S}_r}\text{S}_\text{O}$ codoped SrTiO_3 , it will result in poor photocatalytic activity [see Figs. S1(l) and S1(o)]. The Rh and N orbitals states elevate the VBM of $\text{Rh}_{\text{S}_r}\text{N}_\text{O}$ codoped SrTiO_3 , which results in a band gap of 2.69 eV [see Fig. S1(m)]. The $\text{Mn}_{\text{T}_i}\text{S}_\text{O}$ codoped SrTiO_3 has the band gap of 1.95 eV. The VBM elevation is concomitant with occurrence of S orbitals at VBM and the Mn orbitals at CBm [see Fig. 2(i)]. The shifts in CBm and VBM are such that the band edges straddle the redox potential levels of water. Similarly, for $\text{Mn}_{\text{S}_r}\text{N}_\text{O}$ codoped SrTiO_3 , the band gap is 2.17 eV, and the defect states are shallower, which serves the purpose of efficient photocatalyst [see Fig. S1(n)].

C. Optical properties

The optical spectra has been determined by calculating the frequency dependent complex dielectric function $\epsilon(\omega) = \text{Re}(\epsilon) + \text{Im}(\epsilon)$ using HSE06 functional. The real part $\text{Re}(\epsilon)$ and the imaginary part $\text{Im}(\epsilon)$ are associated with the electronic polarizability and optical absorption of the material, respectively. The sum of all possible transitions from the occupied to the unoccupied states gives the direct interband transition, which is reflected in the imaginary part of the dielectric function. The imaginary and real part for codoped anatase TiO_2 and SrTiO_3 are shown in Fig. 3 (the results for monodoped TiO_2 and SrTiO_3 are shown in Fig. S2). Note that anatase TiO_2 has tetragonal structure. Therefore, the optical anisotropy is also associated with it. The detailed discussion of optical anisotropy is already done in our previous work [78]. Therefore, here we have shown only the averaged (x, y, z polarizations) for imaginary and real part of the dielectric function. The imaginary part of dielectric function shows the first peak at 3.56 eV for pristine TiO_2 as shown in Fig. 3(a) [matching with

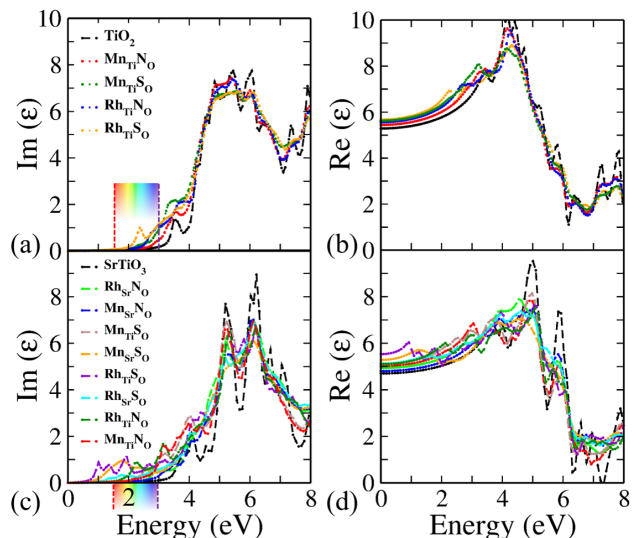


FIG. 3. Spatially average (a) imaginary ($\text{Im } \epsilon$) and (b) real ($\text{Re } \epsilon$) part of the dielectric function for (un)doped TiO_2 , (c) imaginary ($\text{Im } \epsilon$) and (d) real ($\text{Re } \epsilon$) part for (un)doped SrTiO_3 .

the previous works, which is 3.8 eV [79]). The peaks are shifted to lower energy for codoped cases. This enhances the visible light absorption of anatase TiO_2 . The static real part of the dielectric function (at $\omega = 0$) for TiO_2 is found to be 5.28 [see Fig. 3(b)], which is very close to the experimental value i.e., 5.62 [80]. On codoping its value is increased.

For the case of cubic SrTiO_3 , the spatially average imaginary and real part of dielectric function are shown in Figs. 3(c) and 3(d), respectively. The static real part of the dielectric function for pristine SrTiO_3 is estimated as 4.7 (experimental value is 5.27 [81]) and its value is increased with codopants [see Fig. 3(d)]. The first absorption peak is observed at 4.08 eV for pristine SrTiO_3 as shown in Fig. 3(c) [experimental value is 4.7 eV [81]]. Likewise in anatase TiO_2 , the peaks are shifted to visible region for the codoped cases. Note that the optical properties in the high energy range are controlled by the electronic transitions between O 2p states and Ti 3d states. Therefore, the spectra of all the configurations are nearly identical in high energy range. However, the optical properties in low energy range (less than 3 eV) are different, these are affected by the transitions involving the impurity states. The observed visible light absorption could be ascribed to the presence of the dopant states (as shown in DOS near Fermi-level), which reduce the electron transition gap for optical absorption. This leads to a new absorption edge in the visible light region.

D. Band edge alignment

The band edge alignment has been performed to obtain the potential candidates for photocatalytic water split-

ting. The CBm should lie above water reduction potential and VBM should lie below water oxidation potential for overall water splitting. First we align the band edges of pristine TiO_2 and SrTiO_3 w.r.t. water redox potential [47, 48] and further, we align the band edges of defected configurations by observing the shift in CBm and VBM w.r.t. the pristine system [see Fig. 4]. The band edge alignment for monodoped anatase TiO_2 and SrTiO_3 are shown in Fig. S3. The monodoped N_O is not suitable in both the cases (anatase TiO_2 and SrTiO_3), as it results in deep trap states. The latter increases the recombination and decreases the mobility of photogenerated charge carriers [see Fig. S3]. Likewise, for Rh dopant (in monodoping as well as in codoping), there is occurrence of trap states. These states degrade the photocatalytic efficiency. Therefore, mono- and codoping of Rh with a nonmetal could reduce the band gap, but it cannot be an efficient photocatalyst in TiO_2 as well as in SrTiO_3 .

The monodoped S_O in both anatase TiO_2 as well as SrTiO_3 could enhance the photocatalytic efficiency and split water as their band edges straddle the redox potential of water [see Fig. S3]. However, in S_O monodoped SrTiO_3 , the band gap (2.59) is slightly higher than the desirable band gap (~ 2 eV [50, 51]), and thus, its efficiency will be smaller. Similarly, for Mn_{Ti} monodoped SrTiO_3 , the band gap is 2.57 eV, and due to shift of its CBm towards Fermi level, its reduction power will be degraded [see Fig. S3]. On the other hand, for Mn_{Sr} monodoped SrTiO_3 , and Mn_{Ti} monodoped anatase TiO_2 , the slight change in band gap are observed and thus, these can not enhance the photocatalytic activity. In $\text{Rh}_{\text{Ti}}\text{S}_\text{O}$

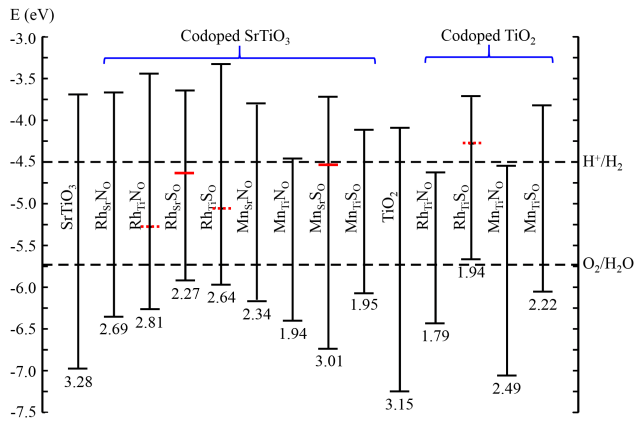


FIG. 4. Band edge alignment of (un)doped SrTiO_3 and TiO_2 w.r.t. water reduction and oxidation potential levels (H^+/H_2 , $\text{O}_2/\text{H}_2\text{O}$). The solid and dashed red line in forbidden region are representing the highest occupied and lowest unoccupied states, respectively.

codoped TiO_2 , since there is manifestation of deep unoccupied states as well as the VBM lies above the oxidation potential of water, it could not be utilized for photocatalytic overall water splitting [see Fig. 4]. For

$\text{Rh}_{\text{Ti}}\text{N}_\text{O}$ and $\text{Mn}_{\text{Ti}}\text{N}_\text{O}$ codoped TiO_2 , the CBm lies below the reduction potential of water, and thus, cannot produce hydrogen via water splitting. In TiO_2 , only the $\text{Mn}_{\text{Ti}}\text{S}_\text{O}$ codoping is the potential candidate for overall photocatalytic water splitting as it has a desirable band gap of 2.22 eV and it does not contain the trap states in forbidden region while retaining the sufficient reduction and oxidation power for hydrogen evolution reaction (HER) as well as oxygen evolution reaction (OER). Similarly, in SrTiO_3 , except $\text{Rh}_{\text{Sr}}\text{N}_\text{O}$, the Rh doping does not aid in enhancing the photocatalytic activity ascribed to the formation of recombination centers. $\text{Rh}_{\text{Sr}}\text{N}_\text{O}$ defect configuration enhances the photocatalytic efficiency, however its band gap (2.69 eV) is little bit larger in comparison to the maximum efficient photocatalyst (~ 2 eV). In $\text{Mn}_{\text{Sr}}\text{S}_\text{O}$, since the occupied deep states lie below the CBm and also these are not the shallow impurity levels, this configuration is not a desirable photocatalyst. The reduction in band gap for $\text{Mn}_{\text{Ti}}\text{N}_\text{O}$ is concomitant with the lowering of CBm, that deteriorates its reduction power. The $\text{Mn}_{\text{Sr}}\text{N}_\text{O}$, and $\text{Mn}_{\text{Ti}}\text{S}_\text{O}$ codoped SrTiO_3 configurations are the potential candidates for overall photocatalytic water splitting attributable to their desirable band gap (~ 2 eV) with congenial band edge positions.

E. Band structure and effective mass

To see the effect on mobility due to the defects, we have calculated the effective mass of charge carriers (using HSE06) of those systems, which could be promising candidates for overall photocatalytic water splitting (see Table I). These are obtained from the relation of effective

TABLE I. Effective masses (in terms of free-electron mass m_e) at the band edges. The masses m_{he} , m_{le} , m_{hh} , and m_{lh} correspond to heavy-electron, light-electron, heavy-hole, and light-hole band, respectively.

Systems	m_{he}	m_{le}	m_{hh}	m_{lh}
pristine SrTiO_3	5.18	0.38	-10.36	-0.74
$\text{Mn}_{\text{Sr}}\text{N}_\text{O}$ codoped SrTiO_3	3.04	-	-	-1.53
$\text{Mn}_{\text{Ti}}\text{S}_\text{O}$ codoped SrTiO_3	-	0.25	-	-0.66
pristine TiO_2	-	0.39	-1.57	-
$\text{Mn}_{\text{Ti}}\text{S}_\text{O}$ codoped TiO_2	-	0.45	-9.23	-
S_O monodoped TiO_2	-	0.41	-2.84	-

mass (m^*) with second derivative of energy with respect to k (wave vector) at the band edges:

$$\frac{1}{m^*} = \frac{1}{\hbar^2} \frac{d^2 E}{dk^2}, \quad (5)$$

where \hbar is the reduced Planck constant. The effective masses of charge carriers of pristine SrTiO_3 are validated with Ref. [82–84]. Except for the heavy hole, all are matching well. For pristine SrTiO_3 , the effective masses are calculated along Γ -X high symmetry path. Pristine has degenerate bands at the Γ k-point [see Fig. 5(a)]. In contrast to pristine SrTiO_3 , rest of the cases have

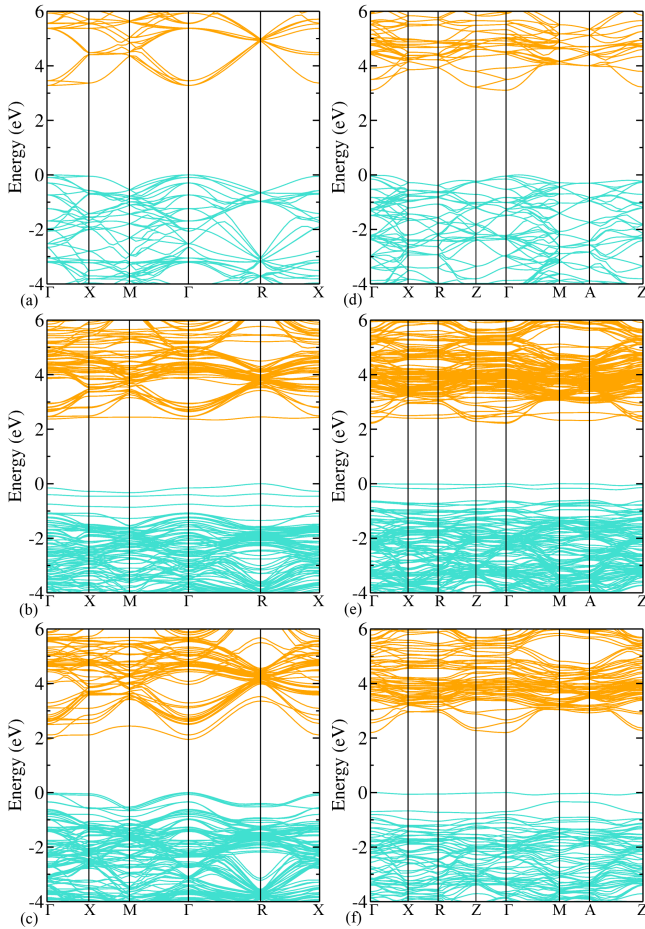


FIG. 5. Band structure calculated using hybrid (HSE06) functional of (a) pristine, (b) $\text{Mn}_{\text{Sr}}\text{N}_{\text{O}}$ codoped [63], (c) $\text{Mn}_{\text{Ti}}\text{S}_{\text{O}}$ codoped SrTiO_3 and (d) pristine, (e) $\text{Mn}_{\text{Ti}}\text{S}_{\text{O}}$ codoped, (f) S_{O} monodoped TiO_2 .

non-degenerate bands (highest occupied and lowest unoccupied) [see Fig. 5]. The electron's effective mass of $\text{Mn}_{\text{Sr}}\text{N}_{\text{O}}$ codoped SrTiO_3 is $3.04m_e$ and $5.09m_e$ along CBm-X and CBm- Γ path, respectively, and the hole's effective mass is $-1.53m_e$ and $-2.58m_e$ along R-X and R- Γ , respectively. These different values along different directions indicate the anisotropic nature of effective mass. For $\text{Mn}_{\text{Ti}}\text{S}_{\text{O}}$ codoped SrTiO_3 , the effective mass of both the charge carriers (calculated along Γ -X direction) is decreased. It is also clear from the large curvature of the bands around CBm and VBM in comparison to pristine SrTiO_3 [see Fig. 5(c)].

In pristine TiO_2 the CBm is at Γ k-point and there is no degeneracy [see Fig. 5(d)]. The electron's effective mass is $0.39m_e$ along Γ -Z high-symmetry path, and the effective mass of hole is $-1.57m_e$ along VBM-Z and $-1.61m_e$ along VBM- Γ direction. For $\text{Mn}_{\text{Ti}}\text{S}_{\text{O}}$ codoped TiO_2 and S_{O} monodoped TiO_2 , the electron's effective mass (along Γ -Z) is comparable with pristine, whereas the hole's effective mass (along VBM-Z) is increased. These increments are also evident from the smaller cur-

vature of the bands around the band edges [see Figs. 5(e) and 5(f)]. For larger effective mass, the mobility will be smaller and the recombination rate will also be greater. Therefore, from Table I, we can see that in case of $\text{Mn}_{\text{Ti}}\text{S}_{\text{O}}$ codoped SrTiO_3 , the mobility of charge carriers will be large, and for rest of the cases, the effective mass values are comparable and the mobility will not be affected much. This is because, the mobility depends on both the effective mass and scattering (relaxation) time. On doping, the scattering rate is expected to get decreased as the degeneracy will be lifted. As a consequence of this, despite of small increment in effective mass, the mobility will not be affected very much especially here the doping concentration is low. These effective mass studies should assist future experimental as well as theoretical investigations to tailor the transport properties of the system.

IV. CONCLUSIONS

In summary, we have evaluated the thermodynamic stability of (un)doped anatase TiO_2 and SrTiO_3 using hybrid DFT and *ab initio* thermodynamics. We have found that the codopants in TiO_2 could act as donor (in p-type host) as well as acceptor (in n-type host). However, the most stable codopants (codoping of metal at Sr site and nonmetal at O site) in SrTiO_3 mostly act as donors. The codoping expands the spectral response and induce visible light in both the cases. However, the recombination centers are present in Rh-related defect configurations attributable to Rh localized orbitals in the forbidden region and moreover, there is a large shift in the CBm or VBM. This will lead to degradation in photocatalytic efficiency. The mobility of charge carriers is maximum in $\text{Mn}_{\text{Ti}}\text{S}_{\text{O}}$ codoped SrTiO_3 , and in rest of the cases, it is not affected much. Our results reveal that $\text{Mn}_{\text{Ti}}\text{S}_{\text{O}}$ codoped, S_{O} monodoped anatase TiO_2 , $\text{Mn}_{\text{Ti}}\text{S}_{\text{O}}$ and $\text{Mn}_{\text{Sr}}\text{N}_{\text{O}}$ codoped SrTiO_3 are the most favorable candidates for enhancing photocatalytic overall water splitting owing to the passivation of trap states and congenial band edge positions with desirable visible light absorption.

ACKNOWLEDGEMENTS

MK acknowledges CSIR, India, for the senior research fellowship [grant no. 09/086(1292)/2017-EMR-I]. PB acknowledges UGC, India, for the senior research fellowship [grant no. 20/12/2015(ii)EU-V]. SS acknowledges CSIR, India, for the senior research fellowship [grant no. 09/086(1231)/2015-EMR-I]. SB acknowledges the financial support from SERB under core research grant (grant no. CRG/2019/000647). We acknowledge the High Performance Computing (HPC) facility at IIT Delhi for computational resources.

-
- [1] X. Chen, S. Shen, L. Guo, and S. S. Mao, *Chemical Reviews* **110**, 6503 (2010).
- [2] A. T. Garcia-Esparza and K. Takanabe, *J. Mater. Chem. A* **4**, 2894 (2016).
- [3] C. Chen, W. Ma, and J. Zhao, *Chem. Soc. Rev.* **39**, 4206 (2010).
- [4] A. Kudo and Y. Miseki, *Chem. Soc. Rev.* **38**, 253 (2009).
- [5] A. Kubacka, M. Fernández-García, and G. Colón, *Chemical Reviews* **112**, 1555 (2012).
- [6] Y. Su, Y. Yang, H. Zhang, Y. Xie, Z. Wu, Y. Jiang, N. Fukata, Y. Bando, and Z. L. Wang, *Nanotechnology* **24**, 295401 (2013).
- [7] T. Takata, C. Pan, and K. Domen, *Science and Technology of Advanced Materials* **16**, 033506 (2015).
- [8] C. Wang, Z. Sun, Y. Zheng, and Y. H. Hu, *J. Mater. Chem. A* **7**, 865 (2019).
- [9] Y. Aoki, M. Sakurai, S. Coh, J. R. Chelikowsky, S. G. Louie, M. L. Cohen, and S. Saito, *Phys. Rev. B* **99**, 075203 (2019).
- [10] Y. Wu, M. K. Y. Chan, and G. Ceder, *Phys. Rev. B* **83**, 235301 (2011).
- [11] G. Fan, X. Wang, H. Fu, J. Feng, Z. Li, and Z. Zou, *Phys. Rev. Materials* **1**, 035403 (2017).
- [12] W.-J. Shi and S.-J. Xiong, *Phys. Rev. B* **84**, 205210 (2011).
- [13] P. Reunchan, N. Umezawa, A. Janotti, J. T-Thienprasert, and S. Limpijumngong, *Phys. Rev. B* **95**, 205204 (2017).
- [14] Y. Gai, J. Li, S.-S. Li, J.-B. Xia, and S.-H. Wei, *Phys. Rev. Lett.* **102**, 036402 (2009).
- [15] R. Long and N. J. English, *Chemistry of Materials* **22**, 1616 (2010), <https://doi.org/10.1021/cm903688z>.
- [16] W.-J. Yin, H. Tang, S.-H. Wei, M. M. Al-Jassim, J. Turner, and Y. Yan, *Phys. Rev. B* **82**, 045106 (2010).
- [17] P. Wang, Z. Liu, F. Lin, G. Zhou, J. Wu, W. Duan, B.-L. Gu, and S. B. Zhang, *Phys. Rev. B* **82**, 193103 (2010).
- [18] C. R. A. Catlow, Z. X. Guo, M. Miskufova, S. A. Shevlin, A. G. H. Smith, A. A. Sokol, A. Walsh, D. J. Wilson, and S. M. Woodley, *Philosophical Transactions of the Royal Society A: Mathematical, Physical and Engineering Sciences* **368**, 3379 (2010).
- [19] Y. Kim, M. Watanabe, J. Matsuda, A. Staykov, H. Kusaba, A. Takagaki, T. Akbay, and T. Ishihara, *J. Mater. Chem. A* **8**, 1335 (2020).
- [20] T. Jafari, E. Moharreri, A. S. Amin, R. Miao, W. Song, and S. L. Suib, *Molecules* **21**, 900 (2016).
- [21] Y. Kuo and K. J. Klabunde, *Nanotechnology* **23**, 294001 (2012).
- [22] B. Modak and S. K. Ghosh, *Phys. Chem. Chem. Phys.* **20**, 20078 (2018).
- [23] Y. Ham, T. Hisatomi, Y. Goto, Y. Moriya, Y. Sakata, A. Yamakata, J. Kubota, and K. Domen, *J. Mater. Chem. A* **4**, 3027 (2016).
- [24] S. K. Kim, W.-D. Kim, K.-M. Kim, C. S. Hwang, and J. Jeong, *Applied Physics Letters* **85**, 4112 (2004).
- [25] B. Liu, H. M. Chen, C. Liu, S. C. Andrews, C. Hahn, and P. Yang, *Journal of the American Chemical Society* **135**, 9995 (2013).
- [26] Y. Wang, R. Zhang, J. Li, L. Li, and S. Lin, *Nanoscale research letters* **9**, 46 (2014).
- [27] X. Ma, X. Cui, Z. Zhao, M. A. Melo, E. J. Roberts, and F. E. Osterloh, *J. Mater. Chem. A* **6**, 5774 (2018).
- [28] R. Konta, T. Ishii, H. Kato, and A. Kudo, *The Journal of Physical Chemistry B* **108**, 8992 (2004).
- [29] H.-C. Chen, C.-W. Huang, J. C. S. Wu, and S.-T. Lin, *The Journal of Physical Chemistry C* **116**, 7897 (2012).
- [30] R. Niishiro, H. Kato, and A. Kudo, *Phys. Chem. Chem. Phys.* **7**, 2241 (2005).
- [31] H. Irie, Y. Watanabe, and K. Hashimoto, *The Journal of Physical Chemistry B* **107**, 5483 (2003).
- [32] T. Ohno, T. Mitsui, and M. Matsumura, *Chemistry letters* **32**, 364 (2003).
- [33] R. Asahi, T. Morikawa, T. Ohwaki, K. Aoki, and Y. Taga, *Science* **293**, 269 (2001).
- [34] C. Di Valentin and G. Pacchioni, *Catalysis today* **206**, 12 (2013).
- [35] Y. Liu, W. Wang, X. Xu, J.-P. Marcel Veder, and Z. Shao, *J. Mater. Chem. A* **7**, 7280 (2019).
- [36] J. Wang, S. Yin, M. Komatsu, Q. Zhang, F. Saito, and T. Sato, *Journal of Photochemistry and Photobiology A: Chemistry* **165**, 149 (2004).
- [37] C. M. Liu, X. T. Zu, and W. L. Zhou, *Journal of Physics D: Applied Physics* **40**, 7318 (2007).
- [38] Y. Y. Mi, S. J. Wang, J. W. Chai, J. S. Pan, C. H. A. Huan, Y. P. Feng, and C. K. Ong, *Applied Physics Letters* **89**, 231922 (2006).
- [39] Y. Guo, X. Qiu, H. Dong, and X. Zhou, *Phys. Chem. Chem. Phys.* **17**, 21611 (2015).
- [40] Y. Lin, Z. Jiang, C. Zhu, X. Hu, X. Zhang, H. Zhu, J. Fan, and S. H. Lin, *J. Mater. Chem. A* **1**, 4516 (2013).
- [41] W. Zhu, X. Qiu, V. Iancu, X.-Q. Chen, H. Pan, W. Wang, N. M. Dimitrijevic, T. Rajh, H. M. Meyer III, M. P. Paranthaman, *et al.*, *Phys. Rev. Lett.* **103**, 226401 (2009).
- [42] J. Wang, H. Sun, J. Huang, Q. Li, and J. Yang, *The Journal of Physical Chemistry C* **118**, 7451 (2014).
- [43] P. Reunchan, S. Ouyang, N. Umezawa, H. Xu, Y. Zhang, and J. Ye, *J. Mater. Chem. A* **1**, 4221 (2013).
- [44] S. Ouyang, H. Tong, N. Umezawa, J. Cao, P. Li, Y. Bi, Y. Zhang, and J. Ye, *Journal of the American Chemical Society* **134**, 1974 (2012).
- [45] R. B. Comes, P. V. Sushko, S. M. Heald, R. J. Colby, M. E. Bowden, and S. A. Chambers, *Chemistry of Materials* **26**, 7073 (2014).
- [46] M. Miyauchi, M. Takashio, and H. Tobimatsu, *Langmuir* **20**, 232 (2004).
- [47] L. Kavan, M. Grätzel, S. E. Gilbert, C. Klemenz, and H. J. Scheel, *Journal of the American Chemical Society* **118**, 6716 (1996).
- [48] Y. Xu and M. A. A. Schoonen, *American Mineralogist* **85**, 543 (2000).
- [49] W. Wei, Y. Dai, M. Guo, L. Yu, and B. Huang, *The Journal of Physical Chemistry C* **113**, 15046 (2009).
- [50] M. G. Walter, E. L. Warren, J. R. McKone, S. W. Boettcher, Q. Mi, E. A. Santori, and N. S. Lewis, *Chemical Reviews* **110**, 6446 (2010).
- [51] V. Stevanović, S. Lany, D. S. Ginley, W. Tumas, and A. Zunger, *Phys. Chem. Chem. Phys.* **16**, 3706 (2014).
- [52] O. Khaselev and J. A. Turner, *Science* **280**, 425 (1998).
- [53] R. Asahi, T. Morikawa, T. Ohwaki, K. Aoki, and Y. Taga, *Science* **293**, 269 (2001).

- [54] X. Chen and C. Burda, *Journal of the American Chemical Society* **130**, 5018 (2008).
- [55] Y. Matsumoto, T. Shimuzu, and E. Sato, *Electrochimica Acta* **27**, 419 (1982).
- [56] B. Liu, H. M. Chen, C. Liu, S. C. Andrews, C. Hahn, and P. Yang, *Journal of the American Chemical Society* **135**, 9995 (2013).
- [57] A. Tkach, P. M. Vilarinho, and A. L. Kholkin, *Acta Materialia* **53**, 5061 (2005).
- [58] H. Yang, P. G. Kotula, Y. Sato, M. Chi, Y. Ikuhara, and N. D. Browning, *Materials Research Letters* **2**, 16 (2014).
- [59] K. Iwashina and A. Kudo, *Journal of the American Chemical Society* **133**, 13272 (2011).
- [60] F. Quan, Y. Hu, X. Zhang, and C. Wei, *Applied Surface Science* **320**, 120 (2014).
- [61] K. D. Lakshmi, T. S. Rao, J. S. Padmaja, I. M. Raju, S. A. Alim, and P. Kalyani, *Environmental Nanotechnology, Monitoring & Management* **10**, 494 (2018).
- [62] P. Basera, S. Saini, E. Arora, A. Singh, M. Kumar, and S. Bhattacharya, *Scientific reports* **9**, 1 (2019).
- [63] M. Kumar, P. Basera, S. Saini, and S. Bhattacharya, *The Journal of Physical Chemistry C* **0**, null (0), <https://doi.org/10.1021/acs.jpcc.9b11160>.
- [64] P. Hohenberg and W. Kohn, *Phys. Rev.* **136**, B864 (1964).
- [65] W. Kohn and L. J. Sham, *Phys. Rev.* **140**, A1133 (1965).
- [66] S. Bhattacharya, D. Berger, K. Reuter, L. M. Ghiringhelli, and S. V. Levchenko, *Phys. Rev. Materials* **1**, 071601 (2017).
- [67] G. Kresse and J. Furthmüller, *Computational Materials Science* **6**, 15 (1996).
- [68] G. Kresse and D. Joubert, *Phys. Rev. B* **59**, 1758 (1999).
- [69] P. E. Blöchl, *Phys. Rev. B* **50**, 17953 (1994).
- [70] A. V. Krukau, O. A. Vydrov, A. F. Izmaylov, and G. E. Scuseria, *The Journal of Chemical Physics* **125**, 224106 (2006).
- [71] T. K. Todorov, S. Singh, D. M. Bishop, O. Gunawan, Y. S. Lee, T. S. Gershon, K. W. Brew, P. D. Antunez, and R. Haight, *Nature communications* **8**, 682 (2017).
- [72] K. van Benthem, C. Elsässer, and R. H. French, *Journal of Applied Physics* **90**, 6156 (2001).
- [73] H. J. Monkhorst and J. D. Pack, *Phys. Rev. B* **13**, 5188 (1976).
- [74] S. Bhattacharya, S. V. Levchenko, L. M. Ghiringhelli, and M. Scheffler, *New Journal of Physics* **16**, 123016 (2014).
- [75] E. Arora, S. Saini, P. Basera, M. Kumar, A. Singh, and S. Bhattacharya, *The Journal of Physical Chemistry C* **123**, 62 (2019).
- [76] A. Bhattacharya and S. Bhattacharya, *Phys. Rev. B* **94**, 094305 (2016).
- [77] T. Ohsawa, I. Lyubinetzky, Y. Du, M. A. Henderson, V. Shutthanandan, and S. A. Chambers, *Phys. Rev. B* **79**, 085401 (2009).
- [78] P. Basera, S. Saini, and S. Bhattacharya, *J. Mater. Chem. C* **7**, 14284 (2019).
- [79] L. Chiodo, J. M. García-Lastra, A. Iacomino, S. Ossicini, J. Zhao, H. Petek, and A. Rubio, *Phys. Rev. B* **82**, 045207 (2010).
- [80] S. H. Wemple, *The Journal of Chemical Physics* **67**, 2151 (1977).
- [81] M. Cardona, *Phys. Rev.* **140**, A651 (1965).
- [82] A. Janotti, D. Steiauf, and C. G. Van de Walle, *Phys. Rev. B* **84**, 201304 (2011).
- [83] M. Marques, L. K. Teles, V. Anjos, L. M. R. Scolfaro, J. R. Leite, V. N. Freire, G. A. Farias, and E. F. da Silva, *Applied Physics Letters* **82**, 3074 (2003).
- [84] M. Fadlallah, M. F. Shibl, T. J. H. Vlugt, and U. Schwingenschlögl, *J. Mater. Chem. A* **6**, 24342 (2018).

Theoretical insights of codoping to modulate electronic structure of TiO_2 and SrTiO_3 for enhanced photocatalytic efficiency

Manish Kumar*, Pooja Basera, Shikha Saini, Saswata Bhattacharya*

Department of Physics, Indian Institute of Technology Delhi, New Delhi 110016 India

*Email: manish.kumar@physics.iitd.ac.in [MK], saswata@physics.iitd.ac.in [SB]

Supplemental Material

- I. Electronic density of states (DOS) of doped anatase TiO_2 and SrTiO_3
- II. Optical properties of monodoped anatase TiO_2 and SrTiO_3
- III. Band edge alignment of monodoped anatase TiO_2 and SrTiO_3

I. Electronic density of states (DOS) of doped anatase TiO_2 and SrTiO_3

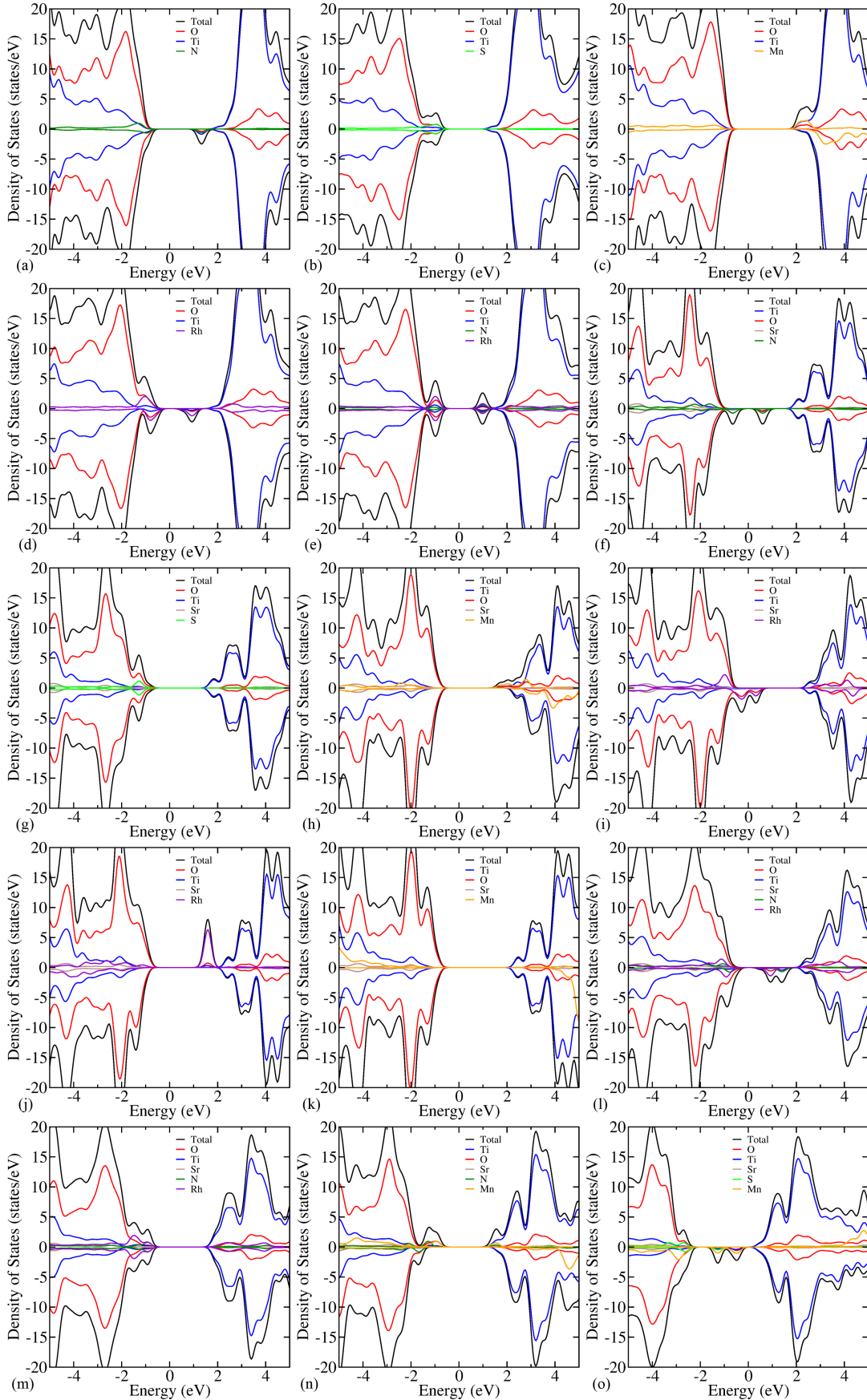


Figure S1: Atom projected density of states of (a) N_O , (b) S_O , (c) Mn_Ti , (d) Rh_Ti (e) $\text{Rh}_\text{Ti}\text{N}_\text{O}$ codoped TiO_2 , and (f) N_O , (g) S_O , (h) Mn_Ti , (i) Rh_Ti , (j) Rh_Sr , (k) Mn_Sr , (l) $\text{Rh}_\text{Ti}\text{N}_\text{O}$, (m) $\text{Rh}_\text{Sr}\text{N}_\text{O}$, (n) $\text{Mn}_\text{Sr}\text{N}_\text{O}$ and (o) $\text{Mn}_\text{Sr}\text{S}_\text{O}$ codoped SrTiO_3 .

II. Optical properties of monodoped anatase TiO_2 and SrTiO_3

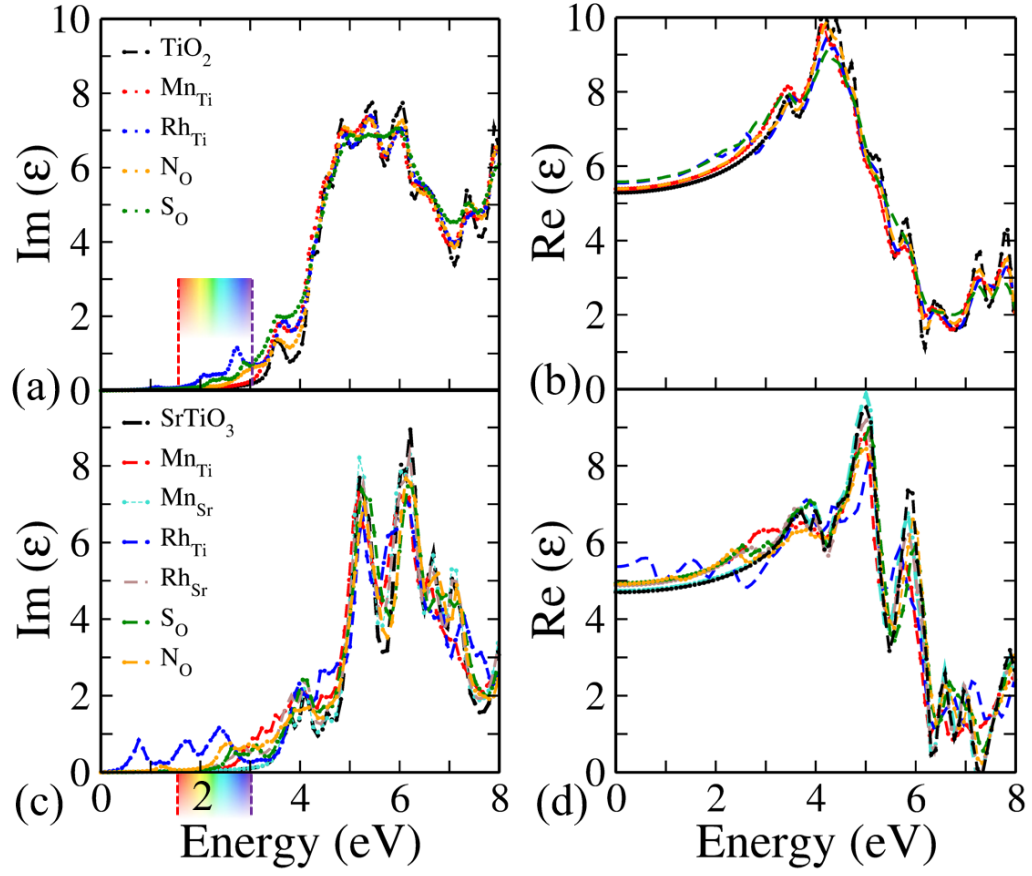


Figure S2: Spatially average (a) imaginary ($\text{Im} \epsilon$) and (b) real ($\text{Re} \epsilon$) part of the dielectric function for (un)doped TiO_2 , (c) imaginary ($\text{Im} \epsilon$) and (d) real ($\text{Re} \epsilon$) part for (un)doped SrTiO_3 .

III. Band edge alignment of monodoped anatase TiO_2 and SrTiO_3

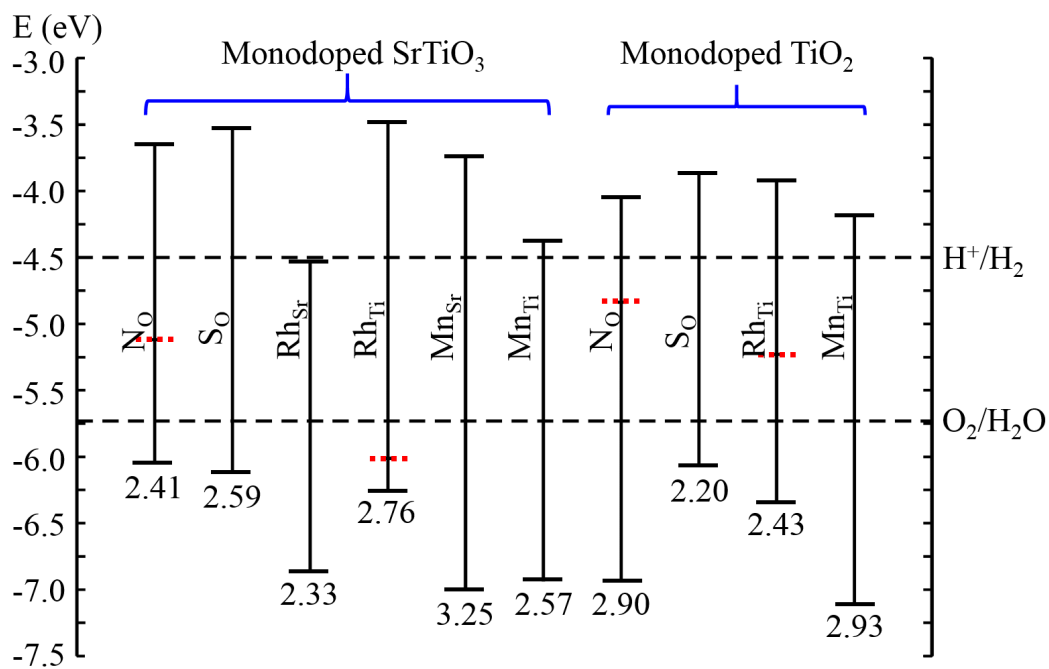


Figure S3: Band edge alignment of monodoped SrTiO_3 and TiO_2 w.r.t. water reduction and oxidation potential levels (H^+/H_2 , $\text{O}_2/\text{H}_2\text{O}$). The dashed red line in forbidden region is representing the lowest unoccupied states.